Chemical Engineering Journal 525 (2025) 170601

Contents lists available at ScienceDirect

Chemical Engineering Journal

journal homepage: www.elsevier.com/locate/cej

Engineering Janus composite electrolytes with catalytic yolk-shell manganese oxide@C nanorods and polyimide frameworks for durable lithium-sulfur batteries

Yun-Sheng Ye [a,d,*], Boy-Yan Xie [a], Wei-Ming Huang [a], Jing-Yu Li [a], Mohamed Gamal Mohamed [a,b], Bing-Joe Hwang [c,d], Shiao-Wei Kuo [a,*]

[a] Department of Materials and Optoelectronic Science, Center of Crystal Research, National Sun Yat-sen University, Kaohsiung, 80424, Taiwan
[b] Chemistry Department, Faculty of Science, Assiut University, Assiut, 71515, Egypt
[c] Department of Chemical Engineering, National Taiwan University of Science and Technology, Taipei, 106335, Taiwan
[d] The Ministry of Education of Taiwan (the Sustainable Electrochemical Energy Development Center (SEED Center)) from the Featured Areas Research Center Program, National Taiwan University of Science and Technology, Taipei, 106335, Taiwan

ARTICLE INFO

Keywords:
Yolk-shell nanorod
Polyimide
Janus composite polymer electrolyte
Li-S battery

ABSTRACT

The practical deployment of lithium-sulfur (Li-S) batteries is hindered by the shuttle effect of lithium polysulfides (LPSs), sluggish redox kinetics, and dendritic lithium growth. Herein, we report a multifunctional Janus composite polymer electrolyte (CPE) featuring a yolk-shell manganese oxide@C nanorod (YSN@C)/polyimide (PI) layer on the cathode-facing side and a porous PI/poly(ethylene oxide) (PEO) layer on the anode-facing side. The YSN@C structure integrates a conductive carbon shell for electron transport and a manganese oxide catalytic core for strong LPS adsorption and accelerated conversion, while the robust PI framework ensures high mechanical strength, thermal stability, and dendrite suppression. Benefiting from synergistic physical confinement, chemical binding, and catalytic activation, the YSN@C/PI/PEO CPE achieves high ionic conductivity, a wide electrochemical stability window (>5.3 V), and superior interfacial compatibility. The resultant cells exhibit high initial capacity (950 mAh g^{-1} at 0.1C, 60 °C), low voltage polarization, excellent rate capability (≥400 mAh g^{-1} at 1.0C), and improved long-term cycling stability (381 mAh g^{-1} after 200 cycles, 40.1 % retention). Density functional theory (DFT) reveal strong Mn_3O_4-LPS binding and favorable Gibbs free energy for multi-step sulfur reduction, consistent with experimental adsorption and catalytic results. This design delivers across-the-board improvements over conventional PEO/Al_2O_3 electrolytes, offering a scalable route toward safe, high-performance solid-state Li-S batteries.

1. Introduction

With the continuous increase in global energy demand and the urgent need for renewable energy storage technologies, lithium-sulfur (Li-S) batteries have garnered significant attention due to their high energy density (2600 Wh kg^{-1}) and theoretical specific capacity (1675 mAh g^{-1}), which far exceed those of conventional Li-S batteries [1]. Furthermore, sulfur, utilized as the cathode material, is abundant, economical, and environmentally sustainable, rendering Li-S batteries a promising next-generation energy storage option [2]. Despite these benefits, the commercialization of Li-S batteries encounters numerous significant obstacles. The soluble lithium polysulfides (LPSs) (Li_2S_n, $4 \leq n \leq 8$) shuttle effect results in a loss of active material and lower cycling stability, whereas the low conductivity of sulfur (≈10^{-30} S cm^{-1}) and lithium sulfide (Li_2S) (≈10^{-13} S cm^{-1}) obstructs effective charge transport [3]. Moreover, substantial volume growth during charge-discharge cycles and the production of Li dendrites on the anode provide considerable safety hazards.

To address the primary challenges posed by the intricate conversion-type reaction of LPSs, which includes $S_8 \rightarrow L_2S_4$ at a higher plateau (≈2.4 V) and $Li_2S_4 \rightarrow Li_2S_2/Li_2S$ at a lowered plateau, the enhancement of electrochemical performance in Li-S batteries through the incorporation of catalytic materials in cathodes and/or on separator surfaces has been extensively investigated [4,5]. Leveraging the unique catalytic

* Corresponding authors at: Department of Materials and Optoelectronic Science, Center of Crystal Research, National Sun Yat-sen University, Kaohsiung, 80424, Taiwan.
E-mail addresses: ysye@mail.nsysu.edu.tw (Y.-S. Ye), kuosw@mail.nsysu.edu.tw (S.-W. Kuo).

https://doi.org/10.1016/j.cej.2025.170601
Received 20 August 2025; Received in revised form 21 October 2025; Accepted 6 November 2025
Available online 7 November 2025

efficacy and favorable adsorption properties of LPSs, metal-based compounds (MCs) and transition metal-based compounds (TMCs) have been utilized in Li-S batteries to enhance the redox transformation of LPSs [6,7]. Recent advances in solid-state electrolytes with catalytic or mechanically reinforced designs have demonstrated promising improvements in Li-metal battery performance [8–10]. These works highlight the importance of interfacial stabilization and catalytic conversion, providing further context for the design rationale adopted in this study. Despite the aforementioned methods achieving some success in mitigating the primary challenges of LPS shuttle and slow conversion, the nonaqueous liquid electrolytes employed in these Li-S batteries remain unstable and highly flammable due to the inclusion of organic solvents (e.g., dioxolane/dimethoxyethane, DOL/DME) [11]. Furthermore, the conventional polyolefin separator employed in liquid electrolyte systems exhibits inadequate affinity for polar electrolytes, resulting in low wettability and adsorption characteristics. This deficiency leads to leakage and compromised stability of Li metal electrodeposition during cycling, thereby posing substantial safety concerns [12].

Polymer-based electrolytes (PEs) are among the most promising alternatives to liquid electrolytes due to their enhanced safety, superior mechanical properties, ease of processing, and cost-effectiveness. Additionally, PEs help mitigate short-circuit risks caused by lithium dendrite growth, while their compatibility with minimal liquid solvents reduces LPS dissolution, thereby effectively suppressing the shuttle effect [13]. However, despite their ability to trap LPS within the polymer backbone, PEs suffer from low ionic conductivity due to the limited segmental mobility of Li-ions in the polymer matrix. To address this challenge, inorganic fillers are incorporated into Li salt-dissolved polymers to form composite polymer electrolyte (CPE), which suppresses polymer chain crystallization and enhances Li-ion transport via surface mechanisms [14]. These fillers can be electrochemically active or inactive, with the bulk phase of active fillers providing additional ion transport pathways alongside the polymer matrix. Specifically, inert fillers (e.g., Al_2O_3, SiO_2) disrupt crystallinity, increasing the fraction of amorphous regions, which facilitates Li-ion mobility [15–17]. Meanwhile, active fillers [e.g., $Li_7La_3Zr_2O_{12}$ (LLZO), $Li_{0.33}La_{0.557}TiO_3$ (LLTO)] exhibit intrinsic ionic conductivity, creating continuous Li-ion transport networks [18,19]. Moreover, surface modifications and 3D nanostructured fillers further optimize Li-ion conduction, reduce interfacial resistance, and improve electrochemical stability at the electrode interface. These advancements make CPEs a highly promising solution for next-generation, solid-state Li-S batteries, enabling higher ionic conductivity, improved mechanical stability, and better suppression of the shuttle effect [20].

Although incorporating inert/or active fillers as reinforcement phases in PEs not only enhances Li-ion conductivity and suppresses Li dendrite growth but also mitigates the shuttle effect of LPSs [21,22]. However, LPSs in CPEs still suffer from sluggish kinetic conversion, causing low sulfur utilization. Therefore, it is essential to build a functional CPE that can effectively address the issues at the cathode and anode interfaces while simultaneously enhancing the reversible redox kinetics of LPS species, which is crucial for the advancement of practical Li-S batteries. Inspired by the Janus separator, which fulfills the all-in-one requirements for both electrodes, they have confirmed that the issues of LPS shuttle and Li metal dendrite growth can be effectively mitigated at the separator-cathode and separator-anode interfaces through the introduction of functional constituents, respectively [23–27]. We utilized a multifunctional Janus CPE to synergistically regulate the anode/cathode interfaces and reversible redox kinetics of LPSs for long-lifespan Li-S batteries. The Janus CPE (YSN@C/PI-PI/PEO) consists of a nanoporous polyimide (PI) impregnated with the polyethylene oxide (PEO)/lithium bis(trifluoromethanesulfonyl)imide (LiTFSI) layer for the Li-anode side and YSN@C/PI with PEO/LiTFSI layer on the S-cathode side, respectively. As illustrated in Scheme 1a, to manufacture the Janus PI-based skeleton, double casting is applied, followed by the nonsolvent-induced phase separation method, and subsequently, infiltration of the PEO/LiTFSI electrolyte is conducted. The cathode interface takes advantage of YSN@C nanorods featuring a one-dimensional yolk-shell architecture, which effectively physically adsorbs LPSs and promotes electron transport via the porous carbon shell with a significant specific surface area, while the manganese oxide core chemically adsorbs and catalyzes LPS, thereby improving the redox reaction kinetics of LPSs (Scheme 1b). The robust PI structure and abundant channels inside the nanoporous PI at the anode contact effectively redistribute Li^+ flux, promoting uniform Li deposition and consequently significantly inhibiting Li dendrite formation. The simultaneous enhancements of the adsorption effect and conversion kinetics effectively inhibit the diffusion of LPSs to the anode, thereby mitigating the corrosion of Li metal. The distinctive structure and streamlined production process of the proposed Janus CPE design are expected to offer significant potential for the advancement of safe Li-S batteries with favorable application prospects.

2. Result and discussion

Herein, the produced manganese oxide@C yolk-shell nanorods (YSN@C), consisting of a yolk-shell nanorod structure, exhibit various distinctive features as functional materials in the CPE close to the cathode side: (i) 1D nanorods serve as nanofillers, promoting the formation of ion-conduction channels in the CPE [15]; (ii) the excellent electrical conductivity of the porous carbon shell enhances the transport of Li ions and electrons, thereby improving the conversion of anchored LPSs [28]; (iii) the inner manganese oxide core functions as a potent chemical adsorbent and an efficient catalyst for LPSs [29,30]. The aforementioned features render YSN@C a viable functional material for practical applications in CPE.

The crystal structure of the as-prepared sample was characterized by X-ray diffraction (XRD). All the diffraction peaks of the precursor sample can be well assigned to high purity α-MnO_2 (JPCDS# 44-0141). As shown in Fig. 1a, the YSN@C is mainly composed of hausmannite Mn_3O_4 with a tetragonal structure (JCPDS# 89-4837) [31]. Additionally, the presence of monoclinic birnessite-type MnO_2 resulting from heating manganese salts/oxides in an alkaline solution at elevated temperatures [29]. The thermogravimetric analysis (TGA) (Fig. 1b) was conducted to determine the carbon content of the materials, revealing mass losses of 9.7 % below 200 °C and 20.1 % between 200 and 400 °C, which correspond to the loss of free water and the combustion of the carbon shell, respectively. To elucidate the decomposition products of the phenol-formaldehyde polymer, the Raman spectra presented in Fig. 1c reveal two peaks at 1320 and 1605 cm^{-1}, corresponding to the D and G bands of carbon, respectively. The intensity ratio of the D band to the G band (I_D/I_G) is around 1, signifying that the shell is composed of amorphous carbon. Furthermore, the high-resolution spectra of C 1S (Fig. 1d) in X-ray photoelectron spectroscopy (XPS) reveal graphite carbon and hydrocarbon at 284.2 and 285.5 eV, respectively. The Mn 2p XPS spectrum had two spin-orbital lines (Fig. S1), corresponding to Mn^{3+} $2p_{3/2}$, Mn^{2+} $2p_{3/2}$, Mn^{3+} $2p_{1/2}$, and Mn^{2+} $2p_{1/2}$ peaks at 640.1, 642.3, 652.9 and 654.1 eV, respectively [32]. The O 1s spectra of YSN@C may be deconstructed into three components with binding energies of 530.4, 531.8, and 533.5 eV (Fig. 1e), corresponding to the lattice oxygen of manganese oxide, the O^{2-} ions of oxygen-vacancy defects within the matrix, and O adsorption on the surface [33]. XPS examination further indicates that the as-prepared samples comprise of amorphous carbon and manganese oxide formed during the calcination process.

To construct a stable PE's matrix, polyimide (PI) was selected as the primary backbone due to its outstanding thermal stability, mechanical robustness, and excellent chemical and electrochemical resistance, which are critical for safe and long-term operation in LMBs [34,35]. Moreover, the structural rigidity and tunable functionality of PI make it an ideal substrate for incorporating porous architectures and ionic components like PEO/LiTFSI. The non-conjugated structure of 1,2,3,4-

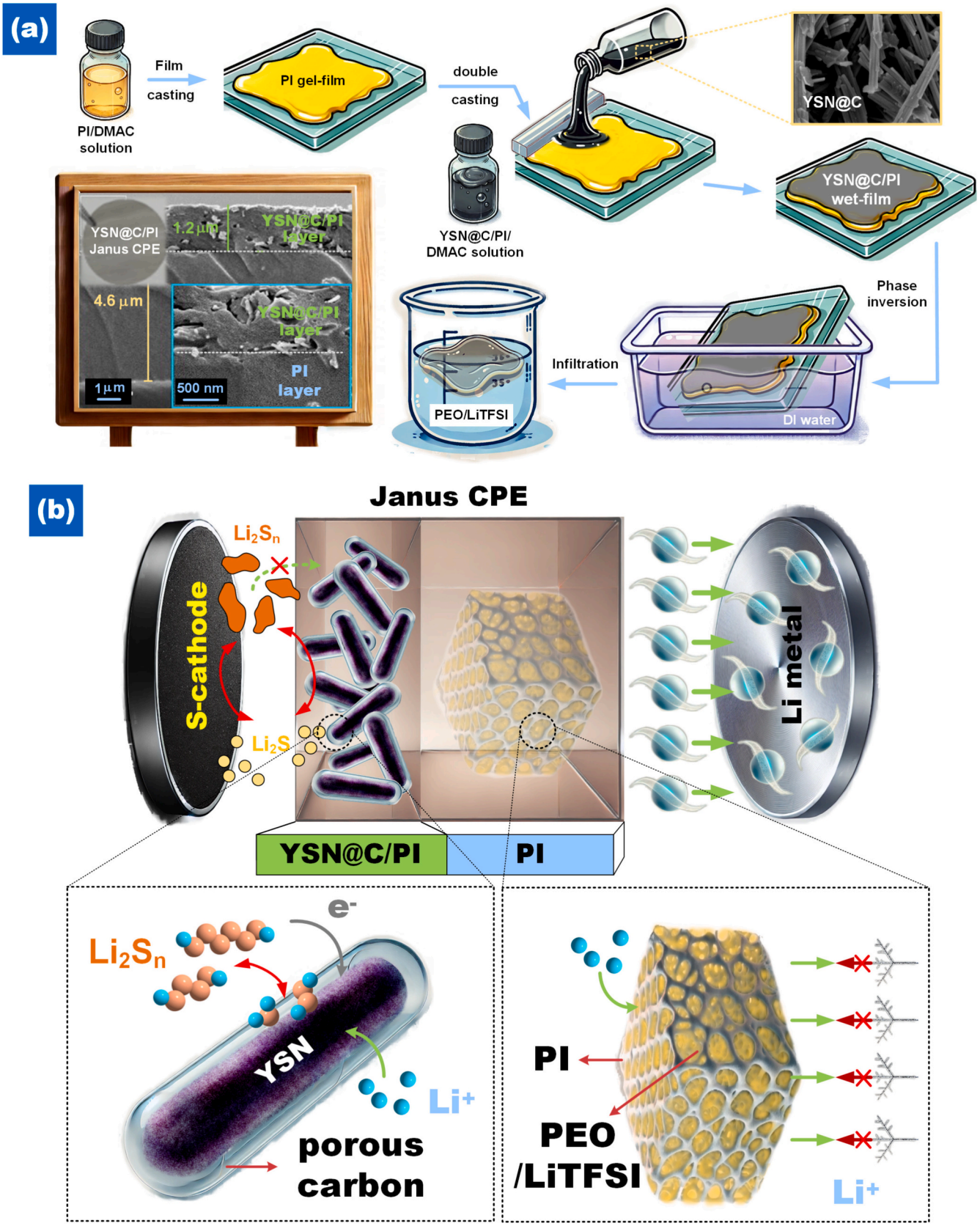

Scheme 1. (a) Synthesis route for the fabrication of YSN@C/PI-PI/PEO Janus CPE; (b) mechanism illustration and basic characterization of YSN@C/PI/PEO Janus CPE: schematic representation of the YSN@C/PI layer on the cathode side and the PI layer on the anode side.

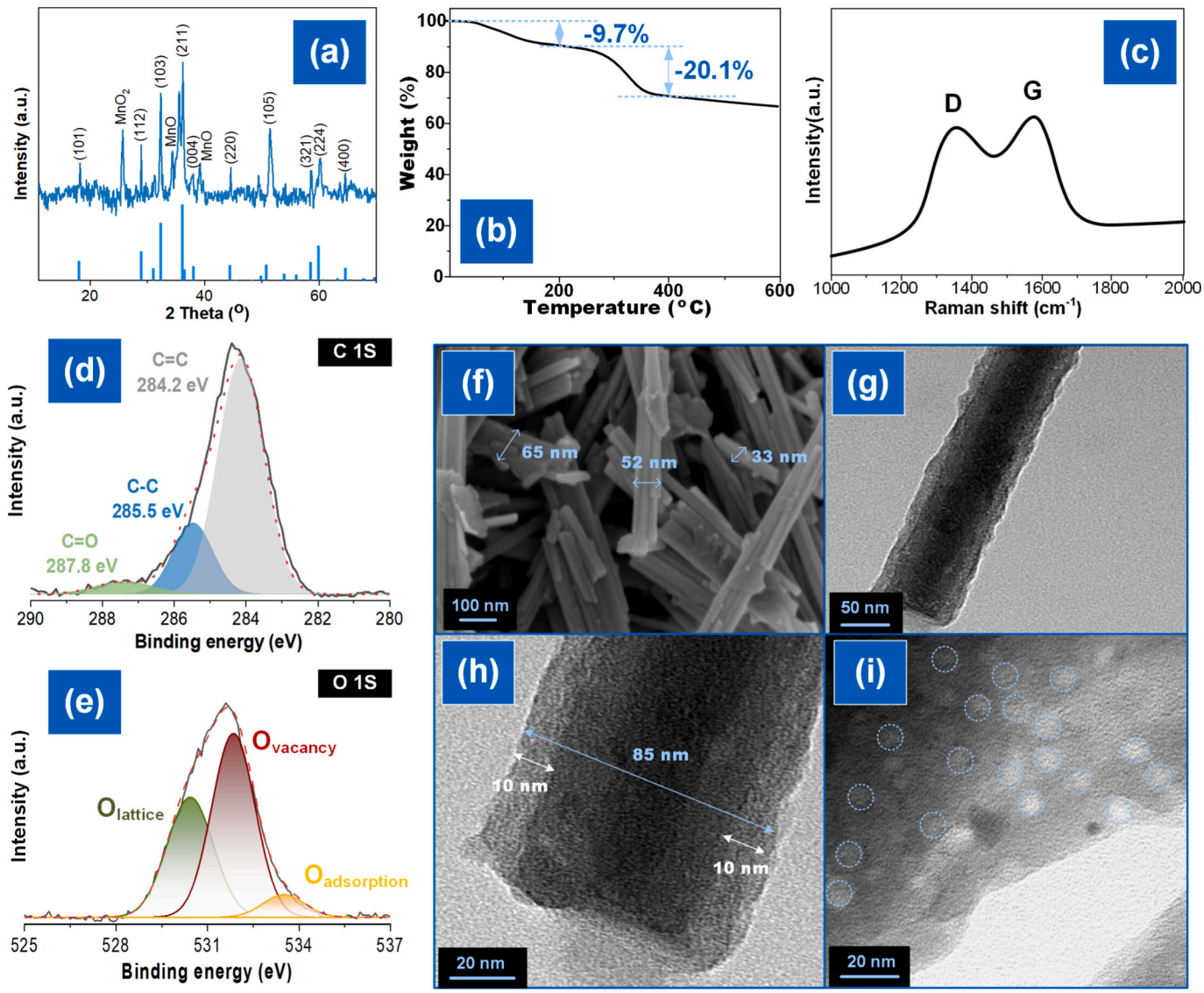

Fig. 1. (a) XRD pattern of α-MnO_2 and YSN@C; TGA curve (b) and (c) Raman spectrum of YSN@C; XPS (d) C 1s and (e) O 1s spectra; SEM images of surface morphology of YSN@C; TEM images of (g, h) YSN@C and (i) porous PI.

cyclobutane tetracarboxylic dianhydride (CBDA) and the fluorinated 4,4′-(hexafluoro isopropylidene) diphthalic anhydride (6FDA) units endowed the synthesized PI with excellent solubility in polar aprotic solvents, enabling effective processing through the NIPS (non-solvent induced phase separation) method. This solubility also allowed for precise structural characterization. ^{1}H NMR analysis (Fig. S2a) revealed characteristic peaks corresponding to the amide (-CONH-) group and aromatic protons (peaks a, b, d, e, f), while the upfield shifts of cyclobutane protons reflected the electron-donating nature of the alicyclic rings. The calculated ratio of AB-TFMB-CBDA to AB-TFMB-6FDA was 6.8:3.2, matching the experimental design. ^{13}C NMR spectra (Fig. S2b) further validated the polymer structure, showing downfield signals for imide and amide carbonyl carbons (peaks 13, 16, 5) and upfield shifts for cyclobutane carbons.

To respectively confirm the yolk-shell architectures of YSN@C and the porous structure of the PI framework, the morphologies of YSN@C and PI were studied using SEM and TEM, as illustrated in Fig. 1f–i. The manganese oxide@C nanorods, measuring several micrometers to several hundred nanometers in length and possessing diameters of 30–100 nm, are observable in Fig. 1f. The TEM images (Fig. 1g and f) demonstrate that the nanorods have a yolk-shell structure, with a clear contrast between the hollow and solid components. The high-magnification TEM image (Fig. 1h) reveals that the carbon shell thickness is approximately 10 nm, but the average core thickness is around 65 nm. On the other hand, the HRTEM image of PI (Fig. 1i) depicted the highly porous structures with pore sizes less than 5 nm, corresponding to the relatively lighter regions and significant porosity throughout the entire PI film [36]. These results confirmed the successful synthesis of a well-defined PI backbone suitable for constructing the PI/PEO CPE system.

The intrinsic lack of ionic conduction in the fabricated PI framework requires careful consideration of the effective penetration of the PEO/LiTFSI electrolyte into the pore structures of the PI. Insufficient PEO content may impede Li-ion transport in the resulting PI and its CPEs, whereas excessive PEO may result in interfacial instability. Therefore, before the fabrication of the Janus CPEs, we first assessed the optimal electrolyte infiltration concentration by adjusting the PEO/LiTFSI solution concentration from 0.75 to 3.0 wt%. Fig. 2a illustrates that the PE content of PI rose from 48.1 % to 91.7 % with increasing PE concentration, but the ionic conductivity (σ) of the resultant PI/PEO CPE remained approximately constant at $\approx 3 \times 10^{-5}$ S cm^{-1} at 60 °C. Besides, the mechanical properties of CPEs were evaluated using tensile strength

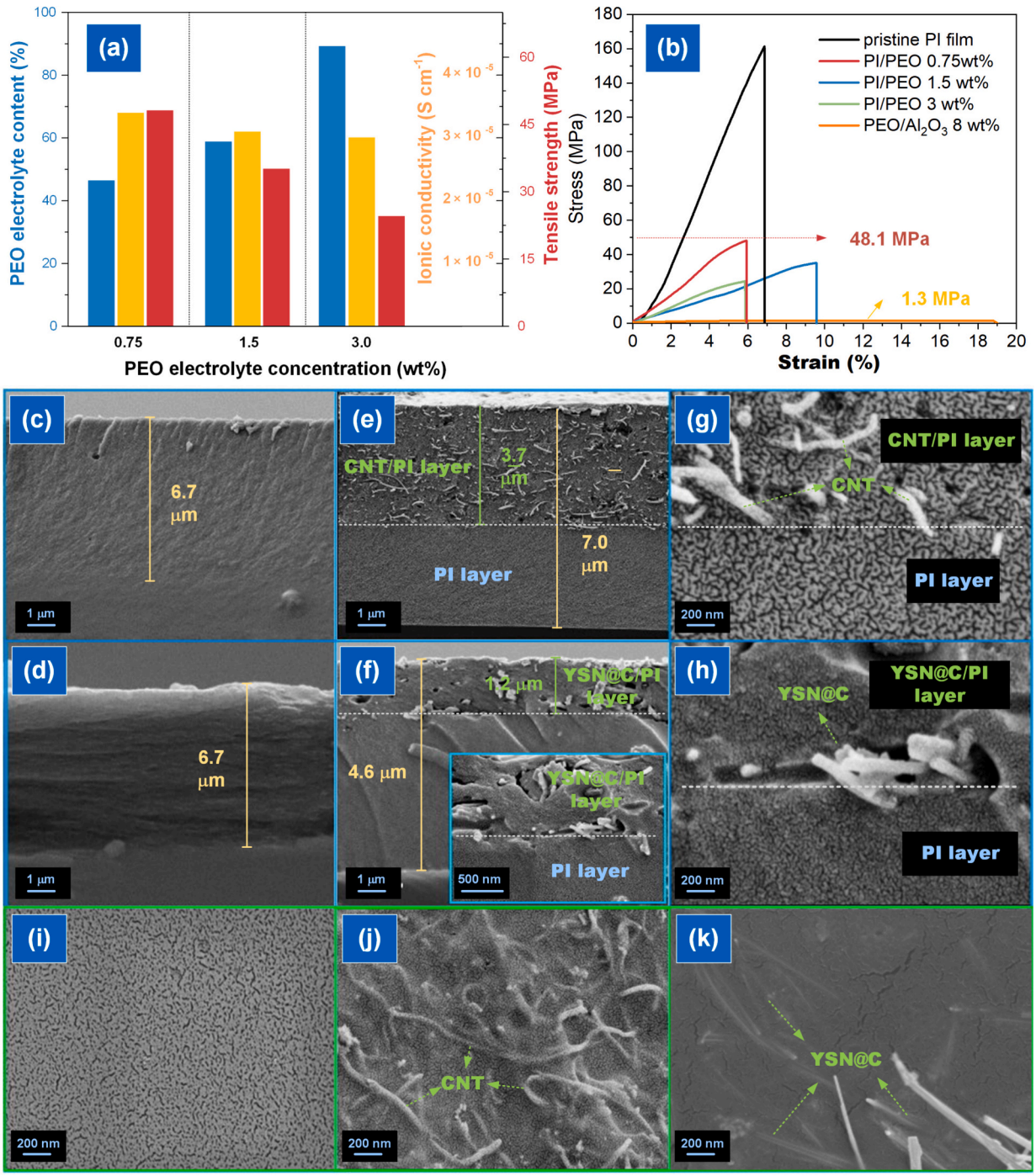

Fig. 2. (a) Effect of PEO/LiTFSI concentration in MeOH on PEO uptake, σ, and tensile strength of the resulting PI/PEO CPE. (b) Stress-strain curves of dense PI, PI/PEO, and PEO/Al_2O_3 8 wt% CPEs. Cross-sectional SEM images of (c) porous PI framework and (d) PI/PEO composite. Cross-sectional SEM images of CNT/PI/PEO Janus CPE at low (e) and high (g) magnification. (f, h) Cross-sectional SEM images of YSN@C/PI/PEO Janus CPE at low (f) and high (h) magnification. (i–k) SEM surface morphologies of Janus CPE layers: (i) pristine PI surface, (j) CNT/PI composite surface, and (k) YSN@C/PI composite surface.

testing, analyzing the stress-strain curves in comparison to pristine PI and PEO/Al_2O_3 at 8 wt%. The dense PI demonstrates an exceptional tensile strength of 162.1 MPa with a strain value of 6.9 %, outperforming that of standard CPE with PEO/Al_2O_3 at 8 wt%, which showed <1.5 MPa. For PI/PEO CPEs, the tensile strength slightly decreases with increasing PE content, which could be attributed to the inherently lower mechanical strength of PE (Fig. 2b). The surface morphologies of the resultant PI/PEO CPEs were examined by SEM (Fig. S3), indicating that at a PE concentration of 3.0 wt%, an uneven and undulating PE layer formed on the smooth PI substrate surface, denoting excessive PE infiltration. According to the aforementioned results, a PE concentration of 1.5 wt% was selected to produce PI-based CPEs and Janus CPEs to provide optimal ionic conductivity, mechanical integrity, and interfacial stability.

The fabrication of Janus CPE was achieved *via* double casting and the NIPS synthesis method, as depicted in Scheme 1a. First, a PI/DMAC solution was coated onto a glass substrate, and after resting, a PI-gel layer formed on the surface. Subsequently, a second coating of PI/DMAC containing 10 wt% YSN@C was applied onto the PI gel layer. Finally, the wet film was sequentially immersed in deionized water and

then in a PEO/LiTFSI solution to fabricate a Janus CPE with a bilayer structure. Similarly, multi-walled carbon nanotubes (CNTs) were employed in the same proportion to replace the YSN@C layer, resulting in the production of the CNT/PI/PEO Janus CPE as a control sample using the identical NIPS and electrolyte infiltration method. Due to the intrinsic coloration of manganese oxide and carbon structures in YSN@C and CNT (Fig. S4), the produced Janus CPE displayed a brown and black color on the YSN@C- or CNT-facing surface.

The produced PI and Janus CPEs were studied by SEM images presented in Fig. 2c–k. The thickness of the porous PI could be regulated to as thin as <7 μm, remaining nearly constant following the penetration of PEO/LiTFSI electrolyte. Conversely, the cross-section of the porous PI exhibits a rather smooth texture, with minimal wrinkles present (Fig. 2c). The prominent bulges observed upon PE infiltration signify that the PE has occupied the pores inside the PI structure (Fig. 2d). The bilayer structure is distinctly seen in the morphology of both Janus separators. The CNT/PI layer (3.7 μm) (Fig. 2e) appears thicker than the YSN@C/PI layer (1.2 μm) (Fig. 2f) due to the higher viscosity of the CNT/PI solution, which leads to a greater actual coating thickness under the same blade-coating conditions. Although the thickness and PEO uptake differ slightly between CNT/PI/PEO and YSN@C/PI/PEO, the superior electrochemical performance of YSN@C/PI/PEO cannot be solely attributed to bulk conductivity. Instead, the yolk-shell catalytic architecture accelerates LPS conversion and provides interfacial confinement, which is the primary origin of the observed enhancement. Further observations from the magnified SEM images (Fig. 2g and h) reveal that both CNT and YSN@C are uniformly embedded within the PI framework. The surface SEM images of the CNT/PI (Fig. 2j) and YSN@C/PI (Fig. 2k) layers in the Janus CPE reveal that tube-like nanomaterials are consistently merged inside the PI structure, which were not found in the PI layer (Fig. 2i). These results suggest that both nanomaterials are well-dispersed in the PI/DMAC solution and can stably co-form with PI into the composite layer during separator fabrication. These 1D nanomaterials facilitate the building of a 3D conductive network, and the distinctive architecture of YSN@C is anticipated to yield synergistic catalytic effects, effectively mitigating the shuttle effect of LPSs and accelerating their conversion.

The mechanical properties of the produced Janus CPEs were evaluated, revealing tensile strengths of 71.8 and 77.6 MPa, with around 6 % strain for CNT/PI/PEO and YSN@C/PI/PEO CPEs, respectively (Fig. 3a). It can be observed that the introduction of a reinforced nanofiller layer in the CPEs enhances the tensile strength of the resulting Janus CPEs compared to the PI/PEO CPE (48.2 MPa and 5.9 %). This improvement is attributed to the uniform dispersion of the nanofillers within the PI

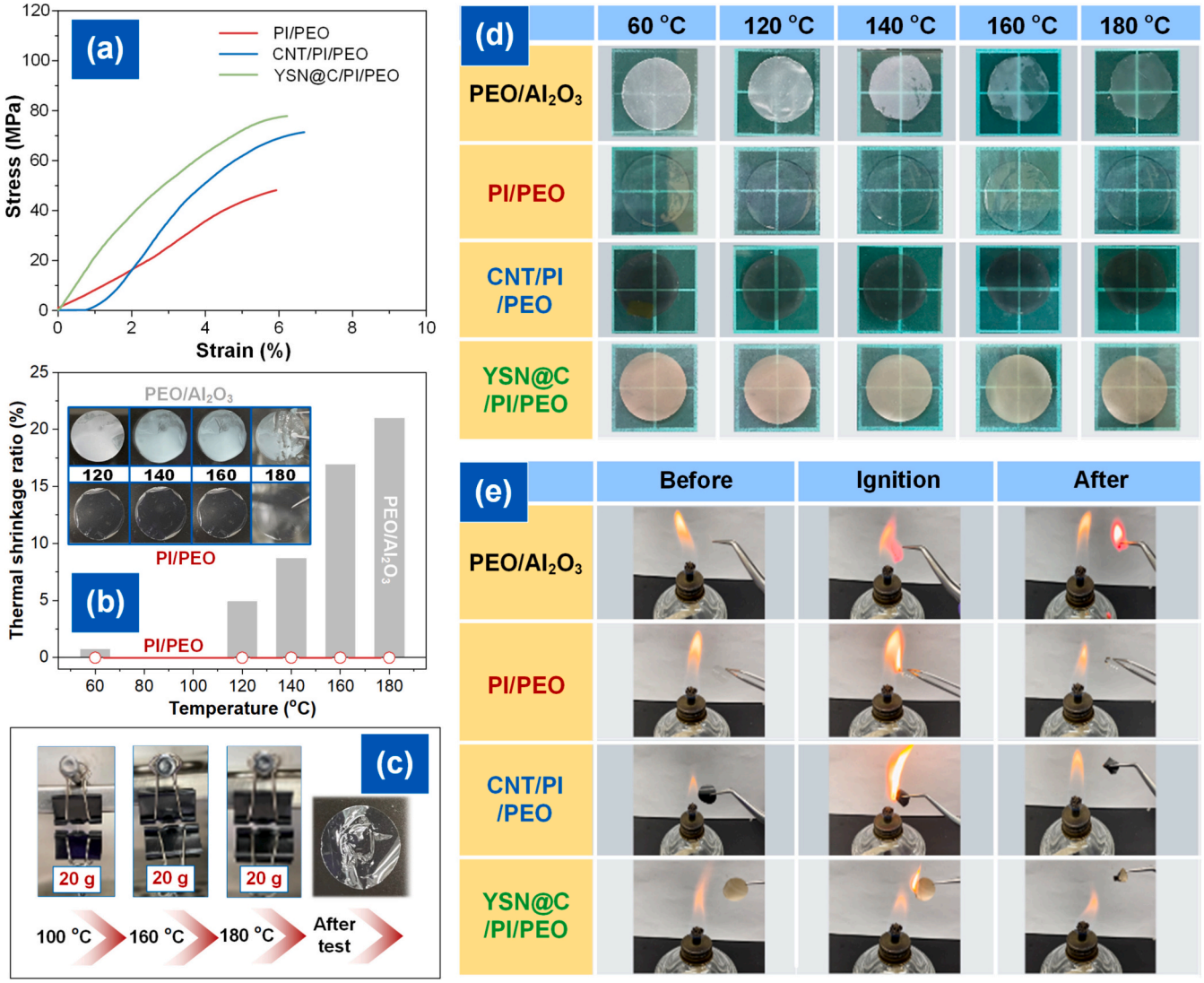

Fig. 3. (a) Stress-strain curves of CPEs; (b) Thermal shrinkage ratio of PEO/Al_2O_3 8 wt% and PI/PEO CPEs; (c) Digital images of the PI/PEO CPE subjected to a 20 g load at various temperatures; (d) Digital images showing the thermal dimensional stability of CPEs at various temperatures; (e) Thermal stability of the CPEs during the combustion process.

matrix, which promotes better load transfer, restricts polymer chain mobility, and mitigates stress concentration under mechanical deformation [37]. The thermal shrinkage properties indicate that the standard PEO/Al_2O_3 8 wt% exhibits a notable rise in thermal shrinkage ratios, rising from 4.8 % to 22.6 % when the temperature increases from 120 to 180 °C (Fig. 3b). Notably, benefiting from the thermally stable PI framework, the PI/PEO CPE exhibits an almost unchanged thermal shrinkage ratio. Furthermore, its σ remains mostly unchanged following temperature testing. When subjected to a 20 g load, the PI/PEO CPE demonstrates excellent mechanical integrity, maintaining its structural completeness even at elevated temperatures up to 180 °C (Fig. 3c). From the digital images, it can also be observed that the PI-based Janus membranes maintain a highly stable shape at various temperatures, with almost no visible thermal shrinkage. During combustion tests, the PI-based CPEs exhibit significantly better flame resistance compared to typical PEO-based CPEs. These results collectively demonstrate the outstanding thermomechanical properties of PI-based CPEs, which are highly beneficial for the development of safer Li metal batteries.

Fig. 3d presents digital photographs of the thermal dimensional stability of various CPEs under elevated temperatures. It can be observed that the incorporation of Al_2O_3 particles significantly enhances the thermal dimensional stability of PEO PE; however, noticeable shrinkage still occurs as the temperature increases. Conversely, the PI-based CPEs, employing the inherent high thermal stability of the PI backbone, demonstrate exceptional dimensional integrity. Both PI/PEO and Janus-structured CPEs retain their form after exposure to 180 °C, exhibiting exceptional thermal resilience. On the other hand, flame tests (Fig. 3e) also reveal that the PEO/Al_2O_3 electrolyte ignites rapidly upon contact with a flame and burns out within a short period. In contrast, the PI backbone provides inherent flame-retardant properties, which help protect the infiltrated PEO PE. Once the flame source is removed, combustion ceases immediately. The results collectively indicate that employing PI as the structural framework confers superior mechanical strength, thermal dimensional stability, and flame resistance to the CPEs.

The TGA curves in Fig. 4a indicate that the dense PI membrane demonstrates the characteristic high thermal stability of PI, with degradation occurring at temperatures above 500 °C. In contrast, the PEO/Al_2O_3 CPE begins to decompose at around 300 °C, which is attributed to the decomposition of the PEO backbone. Benefiting from the thermally stable PI skeleton, the PI-based CPEs show significantly improved thermal resistance. The PI/CNT Janus CPE exhibits more significant thermal degradation below 500 °C, presumably attributable to its higher PEO content.

The σ, Li-ion transference number (t_{Li^+}), and PEO/LiTFSI content of the CPEs are summarized in Fig. 4b. Based on the TGA results, the PEO

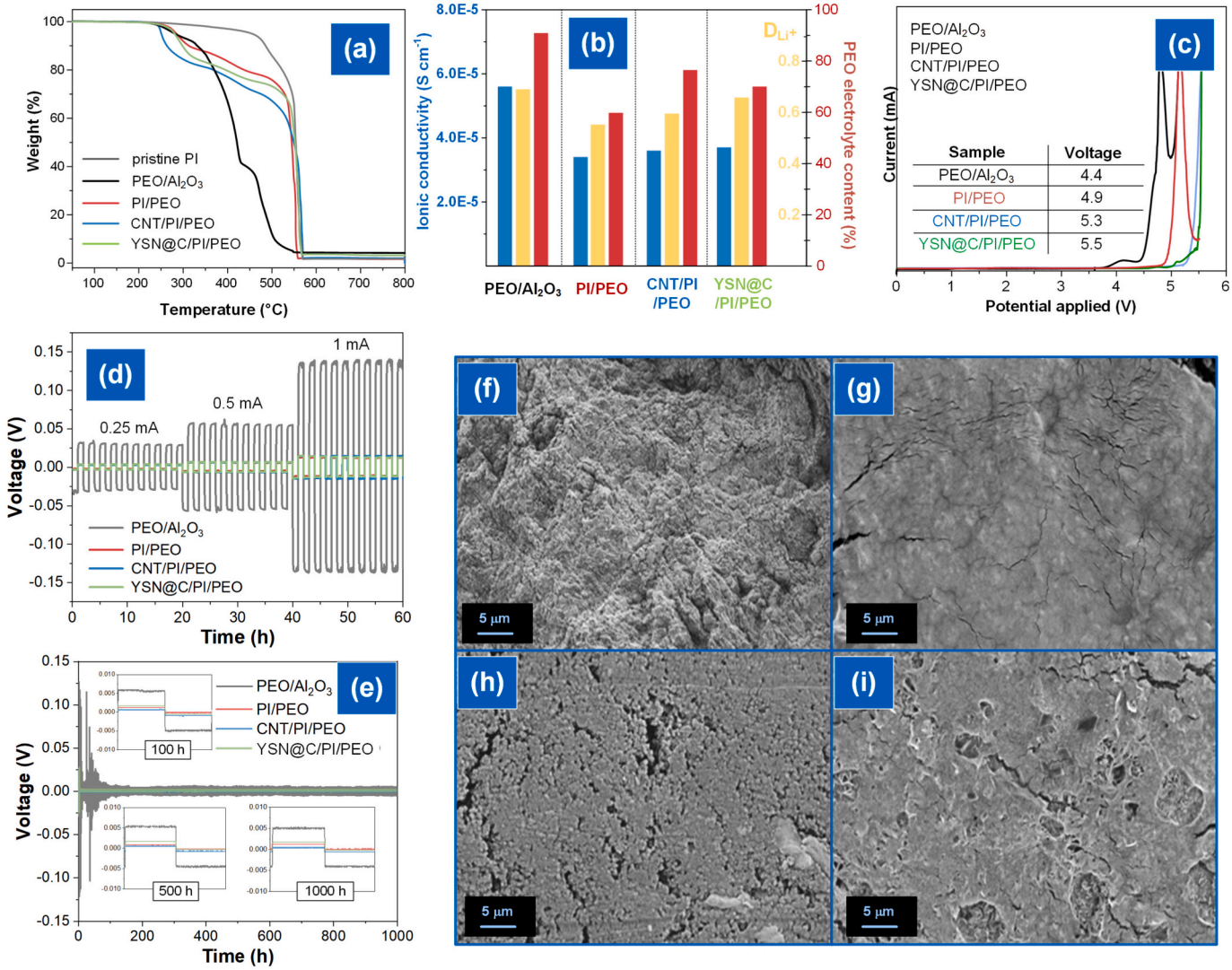

Fig. 4. (a) TGA curves of CPEs. (b) σ, t_{Li^+}, and PEO/LiTFSI content of PEO/Al_2O_3 (8 wt%) and PI-based CPEs. (c) LSV of different CPEs. (d) Galvanostatic cycling at various current densities. (e) Long-term Li|Li symmetric cell cycling at 1 mA cm^{-2} for 1000 h.

content in PI/PEO CPE is 59.5 %. Incorporation of functional layers increases the PEO content to 76.7 % and 70.0 % for CNT/PI/PEO and YSN@C/PI/PEO CPEs, respectively. This enhancement is attributed to the high surface area of the nanomaterials, which create additional voids in the PI framework during NIPS, thereby providing free volume to accommodate the electrolyte. The PEO-based CPE with the highest PEO content (92 %, with Al_2O_3) shows the maximum σ of 5.6×10^{-5} S cm^{-1}. Despite the relatively low PEO content, PI/PEO still achieves $\sigma = 3.3 \times 10^{-5}$ S cm^{-1}, which is further improved when functional layers are introduced, as they provide additional ion conduction pathways surrounding the nanofillers. Fig. S5a–d presents chronoamperometric and impedance results, with calculated t_{Li^+} values of 0.69, 0.55, 0.59, and 0.66 for PEO/Al_2O_3, PI/PEO, CNT/PI/PEO, and YSN@C/PI/PEO, respectively. Notably, the YSN@C/PI/PEO Janus CPE shows a relatively high t_{Li^+} despite its lower PEO content. This suggests that the role of YSN@C is not merely to increase σ, but rather to stabilize interfaces, suppress dendritic growth, and inhibit shuttle effects [38]. Specifically, the Mn—O sites within the yolk-shell Mn_3O_4@C nanorods preferentially coordinate with Li^+, creating selective conduction channels that promote Li^+ migration while effectively hindering anion mobility. This selective interaction explains the higher t_{Li^+} observed for YSN@C/PI/PEO compared with CNT/PI/PEO. Although molecular dynamics simulations could further validate this mechanism, such studies are beyond the current scope and will be pursued in future work. Moreover, the σ of the YSN@C/PI/PEO Janus CPE is comparable to, or even higher than, that of CNT/PI/PEO, confirming the efficacy of the rapid Li^+ conduction percolation network formed by the distinctive yolk-shell nanorods.

The electrochemical operating windows measured by linear sweep voltammetry (LSV) are shown in Fig. 4c. PI/PEO CPEs exhibit a steady platform at 4.9 V, which is much higher than that of PEO/Al_2O_3 (4.4 V). The incorporation of functional layers in the manufactured Janus CPEs results in an elevated decomposition voltage >5.3 V, indicating enhanced electrochemical stability due to resistant nanofillers. The galvanostatic cycling performance of Li|SPE|Li symmetric cells was evaluated at 60 °C, with each current density (0.25, 0.5, and 1 mA) applied for 20 h (Fig. 4d). The symmetric PI-based CPEs assembled cells demonstrate significantly flatter and more symmetric voltage plateaus, with an absolute overpotential of ≈3.5 mV at 0.25 mA, which is lower than that of the symmetric PEO/Al_2O_3 CEP cells, ≈30 mV. This observation indicates that the robust PI framework in CPEs enhances Li stripping and plating with a low voltage polarization. As the current increases to 0.5 and 1 mA, the PI-based CPE-assembled cells exhibit a consistent rise in voltage hysteresis to around 6.5 and 14.0 mV, significantly lower than that of the symmetric cell utilizing PEO/Al_2O_3 CPE (≈57 and ≈138 mV). Furthermore, the Li|SPE|Li symmetric cells are subjected to testing at 1 mA for 1000 h at 60 °C (Fig. 4e). The cell utilizing Pi-based CPEs exhibits a low initial overpotential of ≈28 mV; subsequently, the overpotential gradually declines to around 4 mV, followed by a slow and sustained increase, remaining below 6 mV even after 1000 h. Conversely, the cells with PEO/Al_2O_3 CPE demonstrate a greater initial overpotential (≈127 mV) and maintain a relatively steady overpotential of ≈6 mV up to 165 h; however, noticeable fluctuations in overpotential are observed beyond this point, indicating reduced interfacial stability over prolonged cycling. This exceptionally low polarization is rationalized by three synergistic factors: (i) the ultrathin (~7 μm) thickness of the PI-based CPEs that shortens the Li^+ diffusion path; (ii) the nanoporous PI scaffold that redistributes Li^+ flux and reduces local current density; and (iii) the catalytic YSN@C layer that accelerates interfacial charge transfer. Importantly, the symmetric cells sustain stable cycling for over 1000 h without voltage collapse, and post-cycling EIS spectra (Fig. S6) confirm a finite interfacial resistance, thus excluding the possibility of internal short-circuiting or parasitic electronic conduction. The charge transfer resistance (R_{ct}, semicircle in the EIS spectra) of cells utilizing PI-based CPEs post-cycling is significantly lower than that of the cell employing PEO/Al_2O_3 CPE, suggesting that the incorporation of a PI framework in our PI-based CPEs is advantageous for inhibiting Li dendrite formation. SEM images of the cycled Li metal surface (Fig. 4f–i) reveal substantial irregular Li dendrites on the Li anode of the symmetric cell utilizing the PEO/Al_2O_3 CPE. In contrast, the Li anode of the symmetric cells employing PI-based CPEs exhibits a homogeneous and smooth surface with minimal dendrite formation (Fig. 4g–h). This improvement can be attributed to the enhanced mechanical reinforcement and 3D interconnected nanoporous structure of the PI framework. The porous PI scaffold effectively redistributes Li^+ flux and homogenizes ionic pathways, thereby reducing local current density and suppressing dendritic Li growth at the anode interface. These results confirm that the PI-based architecture not only provides mechanical stability but also plays a critical role in regulating ion transport for uniform Li deposition.

All-solid-state sulfur|CPE|Li batteries using PEO/Al_2O_3, PI/PEO, and Janus CPEs were assembled to verify their stability and electrochemical performances in solid-state batteries (Fig. 5a–c). The charge-discharge curves of the cell with PEO/Al_2O_3 CPE at 0.1C and 60 °C display two distinct voltage plateaus, with the first plateau at around 2.5 V and the second at 2.08 V, reflecting the subsequent reduction of sulfur intermediates. A noticeable decline in the second discharge plateau, linked to the S_8 to Li_2S_n ($n = 4$–8) transformation, is evident with the increasing cycle number due to the LPS shuttle at the evaluated temperature [39]. This behavior is accompanied by an enlarged voltage gap between the high- and low-voltage plateaus, indicating a pronounced loss of LPSs and aggravated kinetic limitations in the transformation of long-chain to short-chain LPSs. The PI/PEO CPE enables a notable increase in the initial discharge capacity to 900 mAh g^{-1}, compared to 660 mAh g^{-1} for the PEO/Al_2O_3 CPE (Fig. 5b). This enhancement is primarily attributed to the significantly thinner thickness (<7 μm) of the PI-based CPE, relative to the ≈50 μm thickness of the PEO/Al_2O_3 CPE, which effectively reduces internal resistance and facilitates improved electrochemical conversion [40]. As cycling progresses, the second discharge plateau gradually diminishes, indicating sluggish LPS conversion kinetics. However, upon introducing a conductive CNT-based functional layer, the CNTs act as an upper current collector positioned on top of the cathode material, facilitating interfacial electron transport and accelerating the redox reactions [41]. This configuration effectively extends the duration of the second discharge plateau during prolonged cycling (Fig. 5c). For the cell with the YSN@C/PI/PEO Janus CPE, it is evident that not only a higher initial capacity (950 mAh g^{-1}) is achieved, but also a smaller voltage gap between the high- and low-voltage plateaus is observed, along with a more gradual capacity decay during cycling. These results indicate that YSN@C, functioning as a multi-functional component, can effectively adsorb and catalyze the conversion of LPSs, thereby mitigating active material loss and enhancing reutilization efficiency.

Fig. 5e displays the potential gap of the cells with different CPEs across various cycles, revealing that the PE-assembled cell exhibits the largest voltage gap and the most pronounced variation over time. In contrast, the cells incorporating YSN@C/PI/PEO Janus CPE shows a smallest voltage hysteresis, indicating reduced overpotential during the discharge process and improved redox kinetics. For the cycling performances in Fig. 5f, both the cells with CNT/PI/PEO and YSN@C/PI/PEO Janus CPEs delivers specific capacity of 280 and 381 mAh g^{-1} after 200 cycles with a capacity retention of 30.9 and 40.1 % at 0.1C under 60 °C, respectively, as compared to PI/PEO CPE (257 mAh g^{-1} and 28.5 %), indicating better cycling stability of Janus structured CPEs. Conversely, the PEO/Al_2O_3 cell exhibits a lower initial specific capacity and poor cycling stability, achieving a specific capacity of 220 mAh g^{-1} after 50 cycles and a significantly reduced specific capacity of ≈100 mAh g^{-1}, with a low-capacity retention of 15.2 % after 200 cycles. An EIS investigation of the cells with varying CPEs before and after prolonged cycling is performed to clarify the resistance linked to ion and electron transfer within the battery. Fig. 5g clearly demonstrates that the PI-based CPEs assembled cells display significantly lower interfacial resistance, as indicated by charge transfer resistance (R_{ct}) associated

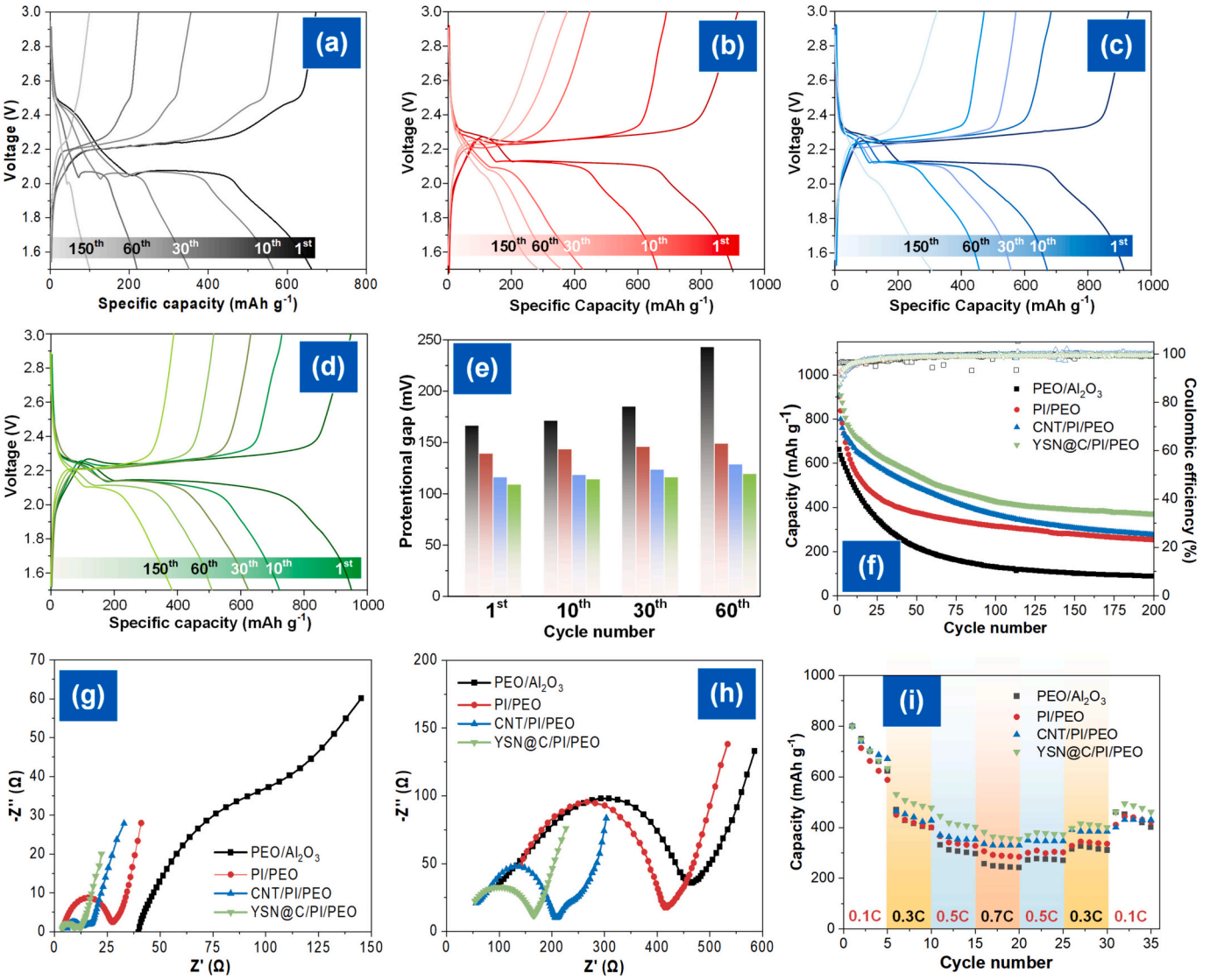

Fig. 5. Charge-discharge profiles of the cells with (a) PEO/Al_2O_3, (b) PI/PEO, (c) CNT/PI/PEO, and (d) YSN@C/PI/PEO. (f) Comparison of the potential gap of the cells with different CPEs at 50 % discharge capacity. (e) Long-term cycling performance and Coulombic efficiency at 0.1C and 60 °C. EIS of the cells with different CPEs (g) before and (h) after cycling, revealing interfacial resistance differences. (i) Rate capability performance of the cells at varying current rates (0.1 to 1.0C), followed by a return to 0.1C at 60 °C.

with electron/ion migration at the electrode/electrolyte interface, before cycling in comparison to the PEO/Al_2O_3 cell, indicating that the PI-based CPEs provide greater interfacial contact with the electrode. However, the cell with PI/PEO CPE reveals a significant change in R_{ct} (ΔR_{ct} = 291.2 Ω) after 200 cycles (Fig. 5h) attributed to the accumulation of intermediate LPSs, resulting in the generation of electrically insulating byproducts at the interface and surface passivation on the Li anode, which obstructs efficient ion and electron transfer [20]. Similar interfacial factors also contribute to a significant increase in R_{ct} for the PEO/Al_2O_3 CPE, with a ΔR_{ct} of 368 Ω. However, owing to the improved interfacial stability, enhanced electron transport, and the effective adsorption and conversion of LPSs, the cell with the YSN@C/PI/PEO CPE exhibits a significantly smaller increase in R_{ct}, with a ΔR_{ct} of only 127.4 Ω.

To evaluate the rate capability of Li-S batteries with different CPEs, galvanostatic charge-discharge measurements were conducted under various current densities ranging from 0.1 to 0.7C under 60 °C. As shown in Fig. 5i, all cells exhibited a gradual decrease in discharge capacity with increasing current rates due to polarization effects and hindered redox kinetics under limited Li-ion transport in the solid-state. Among them, the cell employing the YSN@C/PI/PEO Janus CPE demonstrated the highest overall capacity across the full current range. Notably, it delivered a capacity above 400 mAh g^{-1} even at 1.0C and exhibited rapid recovery to ≈550 mAh g^{-1} when the current rate was switched back to 0.1C, indicating excellent structural and interfacial reversibility. This superior rate performance is attributed to the high σ and LPS conversion efficiency imparted by the conductive YSN@C functional layer. In contrast, the PEO/Al_2O_3 cell exhibited the lowest capacities and poorest capacity recovery, which can be attributed to inferior electrode-electrolyte interfacial contact as well as partial loss of soluble LPSs during cycling. The lack of a conductive or adsorptive functional layer results in inefficient reutilization of active materials and exacerbated redox polarization, ultimately compromising rate capability and long-term reversibility [42]. The multilayer configuration introduces three critical interfaces: YSN@C/PI (catalytic confinement), PI/PEO (mechanical adhesion and ion flux distribution), and PEO/Li (stabilized by the PI scaffold). Although direct interface-resolved tests were not performed, the stable long-term cycling and low hysteresis observed in Li|CPE|Li and Li-S cells indirectly demonstrate favorable interfacial properties.

To further clarify the enhanced electrochemical performances of the PEO/Al_2O_3, PI/PEO, and YSN@C/PI/PEO CPEs in Li-S cells, cyclic voltammetry (CV) tests were performed at various rates (0.1–0.5 mV s^{-1}, Figs. 6a and S7). The CV curves featured two cathodic peaks (S_8 → Li_2S_4 for Peak R1 and Li_2S_4 → Li_2S_2/Li_2S for Peak R2) and one anodic peak (Li_2S_2/Li_2S → S_8 for peak O). The cell with PEO/Al_2O_3 CPE has pronounced peaks for both the redox reactions and a voltage gap of 0.54 V between Peak O and Peak R2. The redox reaction of PI-based CPE, particularly for YSN@C/PI/PEO Janus CPE, exhibits a significantly reduced voltage gap of 0.24 V, indicating diminished polarization and enhanced electrochemical reversibility [43]. The Tafel slopes from the redox peaks (R1, R2, and O) derived from the CV curves of the three

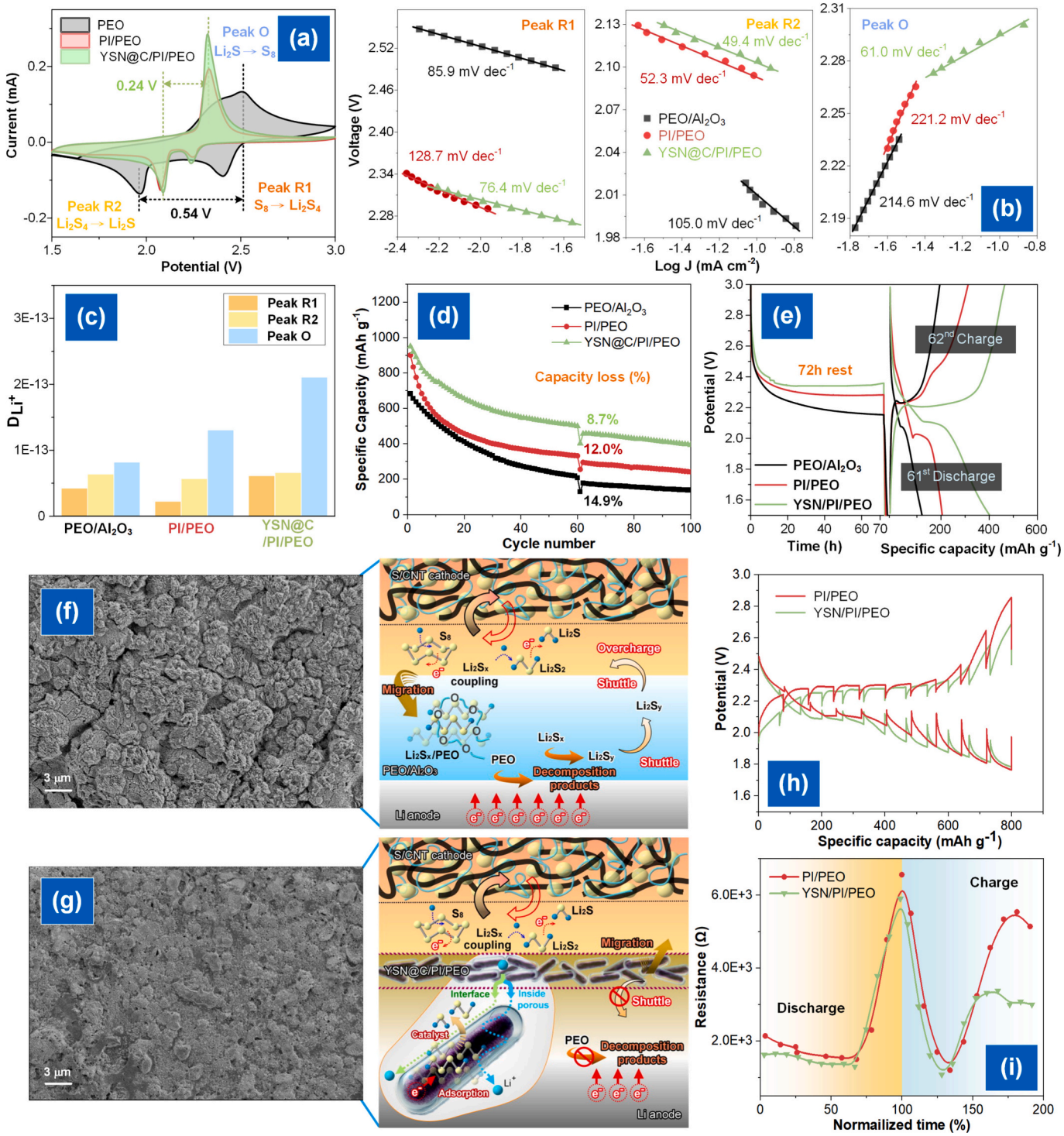

Fig. 6. (a) CV curves of cells with PEO/Al_2O_3, PI/PEO, and YSN@C/PI/PEO CPEs, highlighting redox peaks for LPS conversion, and (b) corresponding Tafel plots for Peak R1, R2, and O. (c) Calculated D_{Li^+} of CPEs derived from CV curves at different peaks. (d) Cycling performance of different cells with a 72 h rest period after the 61st charge at 0.1C. (e) Voltage-time profiles of the cells for the 61st charge and the 62nd discharge cycles at 0.1C. (f) Cycled Li anodes of cells using PEO/Al_2O_3 and YSN@C/PI/PEO CPEs, along with a schematic illustration of the corresponding Li-S battery system. (h) *GITT* curves for the charge-discharge process of cells with PI/PEO and YSN@C/PI/PEO CPE and corresponding (i) IR drop.

CPEs are further analyzed in Fig. 6b. The cell with YSN@C/PI/PEO Janus CPE has the lowest Tafel slope among the three CPEs, especially for Peak O, signifying an enhanced redox reaction. CV curves under different scan rates were measured to reveal the reaction kinetics with respect to the Li-ion diffusion (D_{Li^+}) (Fig. S7). The cell with PEO/Al_2O_3 CPE shows moderate diffusion behavior across all peaks, with D_{Li^+} reaching 8.1 × 10^{-14} cm^2 s^{-1} at Peak O (Fig. 6c). Interestingly, the PI/PEO cell, despite having relatively lower D_{Li^+} at Peak R1, shows comparable or even slightly higher values at Peak R2 and a marked increase at Peak O, reflecting its thinner CPE and stable interfacial characteristics, which help maintain good electrochemical performance even with a lower intrinsic σ. The YSN@C/PI/PEO CPE exhibits the highest D_{Li^+} across all peaks, especially at Peak O where D_{Li^+} exceeds 2.5 × 10^{-13} cm^2 s^{-1}. This highlights the significant role of the YSN@C conductive layer in facilitating rapid Li-ion migration and enhancing the overall redox kinetics. It should be noted that the carbon in YSN@C is confined within the yolk-shell structure and embedded in the PI/PEO matrix, preventing direct electronic contact with Li metal. Four-point probe measurements confirmed negligible bulk conductivity (<10^{-9} S cm^{-1}), indicating that the carbon only contributes to catalytic activity at the cathode side without causing electronic leakage. These results indicate that the YSN@C/PI/PEO CPE offers superior catalytic activity and faster redox kinetics for both the reduction and oxidation of LPSs. The smaller Tafel slopes and D_{Li^+} reflect enhanced charge transfer processes and lower reaction overpotentials, confirming that the introduction of the YSN@C conductive framework facilitates efficient Li-S conversion reactions by providing abundant catalytic sites and improved interfacial electron/ion transport pathways.

To evaluate the self-discharge performance of the cells, a 72-h rest period was introduced between the 61st discharge and the 62nd charge. As shown in Fig. 6d and e, the PEO/Al_2O_3-based cell exhibited a significant capacity loss (14.9 %) and a noticeable voltage drop, indicating severe self-discharge during the idle period. In contrast, the PI/PEO-based cell retained a relatively stable voltage plateau and reduced capacity loss (12 %), suggesting improved suppression of LPS diffusion. Most notably, the YSN@C/PI/PEO Janus CPE cell showed the most stable charge-discharge profile, with minimal voltage drift and the highest retained capacity (8.7 %), demonstrating superior self-discharge resistance. This enhanced performance is attributed to the synergistic effects of the Janus structure and the YSN@C functional layer, which effectively suppresses the shuttle effect and stabilizes the Li-S redox reactions even during prolonged resting states.

To alleviate the adverse impacts of LPSs on the Li anode, a CPE incorporating a YSN@C functional layer and a stiff PI framework is employed as a protective barrier, which can be expected to obstruct the migration of LPSs and their deleterious effects. As shown in Fig. 6f, SEM images reveal the presence of large voids and significant detachment of Li from the surface in the self-discharged cell assembled with the PEO/Al_2O_3 CPE. A rough passivation layer and irregular Li^+ plating/stripping morphology were observed on the cycled Li metal surface in the PEO/Al_2O_3-based cell. In contrast, the Li anode cycled with the YSN@C/PI/PEO CPE exhibited a smooth and uniform morphology (Fig. 6g), indicating more stable and reversible Li^+ deposition behavior. The failure mechanism of both cells is also shown in Fig. 6f and g. Due to the coupling interaction between PEO and LPSs, the cells were more susceptible to the shuttle effect. This interaction also reduced the electrochemical stability of the SPE, as the coupled "PEO-LPSs" structure exhibited a lower LUMO level [44,45]. The introduction of a Janus structure effectively addressed this issue: the YSN@C functional layer facing the S/CNT cathode suppressed LPS shuttle and promoted conversion, while the mechanically robust PI layer facing the Li metal inhibited PEO degradation and enhanced interfacial stability.

The galvanostatic intermittent titration technique (*GITT*) curve was subsequently recorded to evaluate the charge and mass transfer rates during the charge-discharge process from a dynamic perspective, as seen in Fig. 6h. Corresponding reaction resistances at various discharge and charge stages can be determined in Fig. 6i by dividing the overpotential by the pulse current [46]. The results indicate that the reaction resistances of YSN@C/PI/PEO CPE are consistently lower than those of PI/PEO CPE throughout the entire process. The lowered reaction resistance suggests a reduced barrier for Li ion and electron transport throughout the dynamic process, facilitating the capacity activation of the high sulfur cathode [47].

To elucidate the impact of the YSN@C/PI layer on the adsorption and conversion of LPSs, the absorption of YSN@C for Li_2S_6 was initially examined by UV and XPS analyses. As shown in Fig. S8, Li_2S_6 solution was used as a representative soluble LPSs to evaluate the adsorption capacity of YSN@C. After 30 min, the solution immersed in YSN@C turned a soft black, perhaps due to the coloration of YSN@C. Subsequently, the supernatant was further characterized using UV–vis spectroscopy. The prominent absorption peak at 250–350 nm indicates the presence of Li_2S_6, whose intensity significantly decreased in the presence of YSN@C. This finding indicates the substantial adsorbability of YSN@C for LPS capture. The survey XPS spectra depict the surface chemical states of YSN@C following the Li_2S_6 adsorption measurement (Fig. 7a), designated as YSN@C/Li_2S_6. A weak O—Li signal at around 530.5 eV appears following the adsorption of Li_2S_6 in the O 1s spectra of YSN@C, indicating a weak chemical bond between the Li atoms in Li_2S_6 and the O atoms in YSN@C [48]. The Mn^{3+} bonding area increases from 24 % to 37 % following the adsorption of Li_2S_6, but the Mn^{2+} bonding area decreases from 76 % to 63 %, indicating a robust bonding energy between Mn and S atoms in Li_2S_6 (Fig. 7b). Furthermore, the Mn 2p peak moves to a lower binding energy area post-adsorption, signifying that the Mn atom acts as the electron acceptor in the process. The S 2p spectrum identifies four sulfur environments: terminal sulfur (S_T^{-I}), bridging sulfur (S_B^{-I}), thiosulfate (R-SO_2-R/SO_4^{2-}), and polythionate complexes ($S_2O_3^{2-}$/SO_3^{2-}), arranged from low to high binding energy (Fig. 7c) [49]. The latter two complexes involve the oxidation of sulfur species, either during sample transfer or due to the residual presence of LiTFSI. The notable increase in the S_T^{-I}/S_B^{-I} ratio from 0.35 to 0.64 before and after the Li_2S_6 adsorption test unequivocally illustrates the chemical interaction between YSN@C and Li_2S_6.

To evaluate the electrocatalytic performance of YSN@C in the redox reaction of LPSs, CV profiles of the symmetrical cell utilizing a Li_2S_6 solution at a scan rate of 0.5 mV s^{-1} were conducted and are presented in Fig. 7d.The YSN@C curve clearly displays two borders of reversible redox peaks, significantly more apparent than in the cell devoid of Li_2S_6, indicating a notable enhancement in the reaction kinetics of LPSs conversion. A potentiostatic discharge measurement at 2.05 V was conducted to accurately assess the deposition and dissolution kinetics of the Li_2S conversion. Fig. 7e illustrates that the YSN@C/Li_2S_8 electrocatalyst exhibited a larger peak current, achieving its peak at 7124 s, significantly faster than the CNT/Li_2S_8 electrode (10,525 s) with PEO-based PE at 60 °C. The determined capacity contribution of Li_2S deposition is 218 mAh g^{-1} for YSN@C/Li_2S_8, whereas the capacity for CNT/Li_2S_8 is 158 mAh g^{-1}. This suggests that YSN@C facilitates Li_2S activation by promoting rapid charge transfer and effectively immobilizing LPSs around YSN@C, resulting in 3D directional Li_2S precipitation.

First-principles density functional theory (DFT) simulations were conducted to gain deeper insights into the adsorption and reaction mechanisms of LPSs at the molecular and atomic levels. Fig. 7f and g illustrate the optimized adsorption configurations and calculated adsorption energies of various LPS species on graphene and Mn_3O_4 (101) surface, representing the catalytic core components of YSN@C. The adsorption energies for Li_2S, Li_2S_2, Li_2S_4, Li_2S_6, and Li_2S_8 on Mn_3O_4 (101) are calculated as −5.56, −5.88, −5.62, −3.95, and −5.75 eV, respectively, while the adsorption energy for S_8 is predicted to be −1.72 eV. All calculated adsorption energies are negative, thus indicating that the adsorption processes of S_8 and LPS species on the Mn_3O_4 (101) surface are favorable and exothermic. These theoretical calculations are highly consistent with our prior experimental adsorption results, collectively providing valuable insights into how the introduced YSN

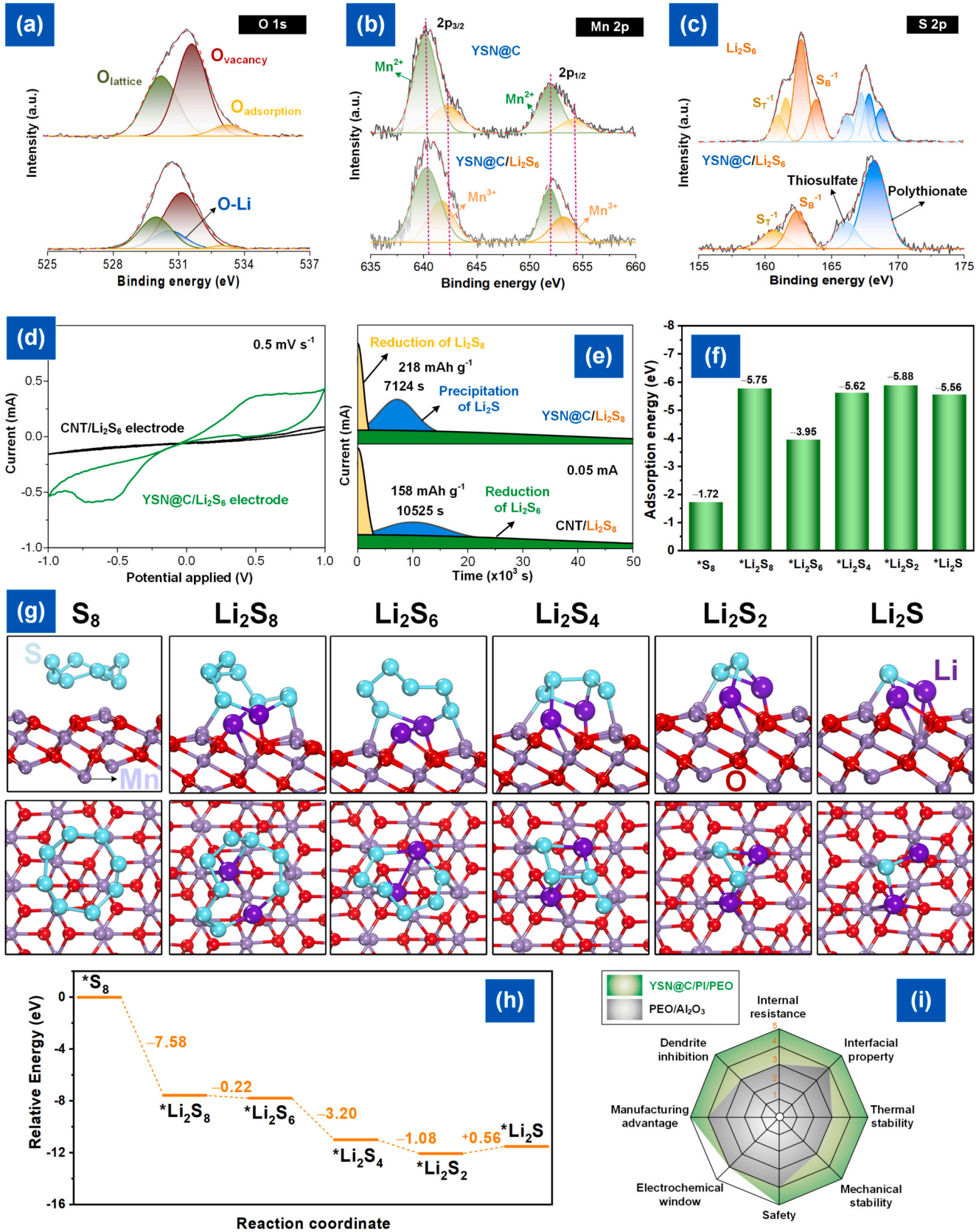

Fig. 7. High-resolution XPS spectra of (a) O 1s, (b) Mn 2P, and (c) S 2p fitting for YSN@C after adsorption of Li_2S_6. (d) CV curves of symmetric cell with CNT/Li_2S_6 and YSN@C/Li_2S_6 electrode. (e) Potentiostatic Li_2S nucleation profiles on CNT/Li_2S_8 and YSN@C/Li_2S_8 electrodes. (f) Computed adsorption energies of S_8 and LPSs on the Mn_3O_4 (101) surface. (g) Schematic illustration of the side (top row) and top (bottom row) views of the most stable geometric configurations of S_8 and LPSs adsorbed on Mn_3O_4 (101) surface. (h) Energy profiles for LPS reduction and Li_2S decomposition. (i) Comparison of the comprehensive performance for PEO/Al_2O_3 and YSN@C/PI/PEO CPEs.

framework governs the adsorption behavior within the YSN@C/PI layer. To further evaluate the thermodynamic feasibility of LPS transformations, the Gibbs free energy (ΔG) for the sulfur reduction reaction (SRR) was calculated according to the transformation equation. As shown in Fig. 7h, S_8 is gradually converted to Li_2S_8 with the ΔG value of −7.58 eV, indicating the reduction step is spontaneous exothermic and easy to occur. Similarly, the reduction of Li_2S_6 to Li_2S_2 is also energetically favorable, while the $Li_2S_2 \rightarrow Li_2S$ step is endothermic ($\Delta G = +0.56$ eV), serving as the rate-determining step of the overall reaction. Notably, when benchmarked against commonly reported Co-, Ni-, and Mo-based catalysts (adsorption energies typically in the range of −4.5 to −6.0 eV) [50,51], Mn_3O_4 demonstrates comparable binding strength toward LPSs, but with the advantages of lower cost, reduced toxicity, and better stability. These combined results underscore that Mn_3O_4 provides both strong polysulfide anchoring and favorable catalytic kinetics, making it a uniquely practical and sustainable catalytic choice for Li-S batteries [49,52].

Finally, when benchmarked against conventional PEO/Al_2O_3 CPEs, the YSN@C/PI/PEO demonstrates across-the-board superiority in eight critical performance dimensions (Fig. 7i). Specifically, it exhibits markedly lower internal resistance, enhanced interfacial compatibility, and exceptional thermal and mechanical stability, key attributes for long-term LMBs operation. The Mn_3O_4-based YSN architecture provides effective dendrite suppression and broad electrochemical window stability, while simultaneously maintaining a high safety margin and manufacturing scalability. This synergistic balance of electrochemical performance, structural integrity, and process feasibility not only surpasses the PEO/Al_2O_3 benchmark in every evaluated category but also highlights the strategic integration of catalytic Mn_3O_4, conductive carbon, and robust PI substrate. These combined advantages position YSN@C/PI/PEO as a next-generation multifunctional separator capable of meeting the stringent demands of high-energy-density LMBs and potentially extending to other advanced battery chemistries.

3. Experimental section

Synthesis of porous polyimide (PI) [36]: PI was synthesized via a conventional two-step polycondensation and thermal imidization procedure. Initially, AB-TFMB (10.0 g, 17.9 mmol) was dissolved in *N*,*N*-dimethylacetamide (DMAc, 133 g) under a N_2 atmosphere at room temperature with continuous stirring until a homogeneous solution was obtained. Subsequently, CBDA (2.46 g, 12.53 mmol) and 6FDA (2.39 g, 5.37 mmol) were gradually added to the solution, and the resulting mixture was stirred for 18 h to form a poly(amic acid) (PAA) precursor. After the completion of the polymerization, acetic anhydride (12.2 g) and pyridine (6.3 g) were added to the reaction mixture as chemical dehydrating agents. The temperature was then increased to 80 °C, and the solution was stirred for an additional 12 h to promote the imidization reaction and obtain PI. Upon completion, the reaction mixture was cooled to room temperature and slowly poured into a 1:1 (v/v) water/alcohol solution to precipitate the PI fibers. The precipitated fibers were collected by filtration, washed thoroughly, and then dried in a vacuum oven at 50 °C for 24 h to remove residual solvents and complete the imidization process.

Preparation of PI/PEO CPE: The PI/PEO CPE was prepared by a NIPS process to form a porous PI framework, followed by infiltration with a PEO/LiTFSI solution ([EO]:[Li] = 10:1). Detailed solvent casting, phase inversion, and infiltration procedures are provided in the Supporting Information.

Synthesis of manganese oxide@C yolk-shell nanorod (YSN@C): YSN@C was synthesized via a three-step process involving hydrothermal synthesis, polymer coating, and carbonization. Briefly, MnO_2 nanorods were first prepared through a hydrothermal reaction, followed by resorcinol-formaldehyde polymer coating and subsequent carbonization under N_2. Finally, the silica component was removed by NaOH etching to yield yolk-shell Mn_3O_4@C nanorods. Detailed washing, solvent exchange, and drying procedures are provided in the Supporting Information.

Fabrication of Janus CPEs: The YSN@C/PI/PEO Janus CPE was fabricated by a double-casting and NIPS method. A PI/YSN@C casting solution was prepared and sequentially coated on a glass substrate to form the Janus framework, followed by PEO/LiTFSI infiltration to obtain the final CPE. For comparison, CNT/PI/PEO and PI/PEO CPEs were prepared using the same procedure, with CNTs or no filler added, respectively. Detailed compositions, casting parameters, and infiltration procedures are provided in the Supporting Information.

Preparation of sulfur cathode: The sulfur-carbon (S/CNT) composite was prepared by mixing activated carbon (AC), black carbon, CNTs, and elemental sulfur powder in a mass ratio of 3:1:1:5. The mixture was ground thoroughly in a mortar for 30 min to ensure uniform dispersion. The resulting powder was then transferred into a glass tube, sealed under vacuum using a gas blowtorch, and subjected to a thermal treatment at 155 °C for 8 h to facilitate sulfur infusion, yielding the S/C composite. To fabricate the cathode slurry, 5 wt% of the S/C composite, 30 wt% of poly(vinylidene fluoride) (PVDF), and 20 wt% of LiTFSI were dispersed in NMP using mechanical stirring for 1 h to obtain a homogeneous suspension. The slurry was then coated and punched into 12 mm diameter electrode discs, with an average sulfur mass loading of approximately 2.0 mg cm^{-2}.

Battery assembly: Prior to assembly, the CPEs were cut into circular discs with a diameter of 16 mm, and the electrodes into 12 mm discs. These components were dried in a vacuum oven at 70 °C for 4 h to remove residual moisture. After drying, the materials were transferred into an argon-filled glovebox with H_2O and O_2 levels maintained below 0.5 ppm. Inside the glovebox, Li metal foil (thickness: 0.45 mm, diameter: 15.8 mm) was prepared as the anode. Coin-type cells (CR2032) were assembled following the sequence: positive case, cathode, CPE, Li metal anode, stainless steel spacer, spring, and negative case. The assembled cells were then sealed using a battery crimping machine. After sealing, the cells were thermally aged at 60 °C for 4 h before electrochemical testing.

4. Conclusions

In summary, we have successfully engineered multifunctional Janus composite electrolytes (CPEs) featuring a catalytic YSN@C/PI layer on the cathode side and a porous PI/PEO layer on the anode side. This asymmetric design integrates strong polysulfide confinement, catalytic activation, and mechanical reinforcement into a single architecture. As a result, the Janus CPEs exhibit high ionic conductivity, a wide electrochemical stability window (>5.3 V), and excellent interfacial compatibility. The assembled Li-S cells deliver a high initial capacity of 950 mAh g^{-1}, superior rate performance, and enhanced cycling stability, maintaining 381 mAh g^{-1} after 200 cycles with 40.1 % retention at 0.1C and 60 °C. Although the present work demonstrates stable cycling up to 200 cycles, the exceptionally low polarization in symmetric Li|Li cells (>1000 h) and the minimal increase in charge-transfer resistance (ΔR_{ct} = 127.4 Ω) strongly suggest that the Janus CPE system can sustain performance for extended operation. These findings provide compelling evidence that the Janus CPE architecture has significant potential to maintain durable electrochemical performance over ≥500 cycles in future evaluations. Overall, the combination of catalytic confinement, structural robustness, and interfacial stability positions the YSN@C/PI/PEO Janus CPE as a promising electrolyte platform for the development of safe and high-performance Li-S batteries.

CRediT authorship contribution statement

Yun-Sheng Ye: Writing – review & editing, Writing – original draft, Supervision, Resources, Investigation, Conceptualization. **Boy-Yan Xie:** Methodology, Investigation, Data curation. **Wei-Ming Huang:** Investigation, Formal analysis. **Jing-Yu Li:** Methodology, Formal analysis.

Mohamed Gamal Mohamed: Validation, Investigation. **Bing-Joe Hwang:** Resources, Conceptualization. **Shiao-Wei Kuo:** Supervision, Resources.

Declaration of competing interest

The authors declare the following financial interests/personal relationships which may be considered as potential competing interests: Yun-Sheng Ye reports financial support was provided by National Science and Technology Council. If there are other authors, they declare that they have no known competing financial interests or personal relationships that could have appeared to influence the work reported in this paper.

Acknowledgements

We acknowledge financial support from the National Science and Technology Council (NSTC) (112-2222-E-110-007-MY2, 114-2221-E-110-009-MY3, 114-2639-E-011-001-ASP) and analytical assistance from the Instrumentation Center at National Sun Yat-sen University.

Appendix A. Supplementary data

Supplementary data to this article can be found online at https://doi.org/10.1016/j.cej.2025.170601.

Data availability

Data will be made available on request.

References

[1] B.-J. Lee, C. Zhao, J.-H. Yu, T.-H. Kang, H.-Y. Park, J. Kang, Y. Jung, X. Liu, T. Li, W. Xu, X.-B. Zuo, G.-L. Xu, K. Amine, J.-S. Yu, Development of high-energy non-aqueous lithium-sulfur batteries via redox-active interlayer strategy, Nat. Commun. 13 (1) (2022) 4629, https://doi.org/10.1038/s41467-022-31943-8.
[2] L. Zhou, D.L. Danilov, R.-A. Eichel, P.H.L. Notten, Host materials anchoring polysulfides in Li–S batteries reviewed, Adv. Energy Mater. 11 (15) (2021) 2001304, https://doi.org/10.1002/aenm.202001304.
[3] H. Kim, J.T. Lee, A. Magasinski, K. Zhao, Y. Liu, G. Yushin, In situ TEM observation of electrochemical lithiation of sulfur confined within inner cylindrical pores of carbon nanotubes, Adv. Energy Mater. 5 (24) (2015) 1501306, https://doi.org/10.1002/aenm.201501306.
[4] Y.C. Jeong, J.H. Kim, S. Nam, C.R. Park, S.J. Yang, Rational design of nanostructured functional interlayer/separator for advanced Li–S batteries, Adv. Funct. Mater. 28 (38) (2018) 1707411, https://doi.org/10.1002/adfm.201707411.
[5] B. Yan, X. Li, W. Xiao, J. Hu, L. Zhang, X. Yang, Design, synthesis, and application of metal sulfides for Li–S batteries: progress and prospects, J. Mater. Chem. A 8 (35) (2020) 17848–17882, https://doi.org/10.1039/D0TA06220K.
[6] X. Zhu, Recent advances of transition metal oxides and chalcogenides in pseudo-capacitors and hybrid capacitors: a review of structures, synthetic strategies, and mechanism studies, J. Energy Storage 49 (2022) 104148, https://doi.org/10.1016/j.est.2022.104148.
[7] B. Guan, X. Gao, Z. Wang, K. Sun, A review of metal phosphides with catalytic effects in Li–S batteries: boosting the redox kinetics, Nanoscale 16 (23) (2024) 11005–11018, https://doi.org/10.1039/D4NR01520G.
[8] J. Peng, D. Lu, S. Wu, N. Yang, Y. Cui, Z. Ma, M. Liu, Y. Shi, Y. Sun, J. Niu, F. Wang, Lithium superionic conductive nanofiber-reinforcing high-performance polymer electrolytes for solid-state batteries, J. Am. Chem. Soc. 146 (17) (2024) 11897–11905, https://doi.org/10.1021/jacs.4c00882.
[9] T. Zhang, L. Liu, Z. Zou, Z. Zeng, B. Li, Z. Li, Z. Ren, X. Cheng, X. Feng, Z. Wang, M. Liu, P. Wang, J. Niu, 3D printing zwitter molecule-enhanced solid polymer electrolytes for high-energy lithium metal batteries, Adv. Funct. Mater. 35 (22) (2025) 2424362, https://doi.org/10.1002/adfm.202424362.
[10] L. Liu, Y. Shi, M. Liu, Q. Zhong, Y. Chen, B. Li, Z. Li, T. Zhang, H. Su, J. Peng, N. Yang, P. Wang, A. Fisher, J. Niu, F. Wang, An ultrathin solid electrolyte for high-energy lithium metal batteries, Adv. Funct. Mater. 34 (39) (2024) 2403154, https://doi.org/10.1002/adfm.202403154.
[11] Z. Song, F. Chen, M. Martinez-Ibañez, W. Feng, M. Forsyth, Z. Zhou, M. Armand, H. Zhang, A reflection on polymer electrolytes for solid-state lithium metal batteries, Nat. Commun. 14 (1) (2023) 4884, https://doi.org/10.1038/s41467-023-40609-y.
[12] X. Yu, A. Manthiram, A review of composite polymer-ceramic electrolytes for lithium batteries, Energy Storage Mater. 34 (2021) 282–300, https://doi.org/10.1016/j.ensm.2020.10.006.
[13] J. Qian, B. Jin, Y. Li, X. Zhan, Y. Hou, Q. Zhang, Research progress on gel polymer electrolytes for lithium-sulfur batteries, J. Energy Chem. 56 (2021) 420–437, https://doi.org/10.1016/j.jechem.2020.08.026.
[14] A.L. Mong, Q.X. Shi, H. Jeon, Y.S. Ye, X.L. Xie, D. Kim, Tough and flexible, super ion-conductive electrolyte membranes for lithium-based secondary battery applications, Adv. Funct. Mater. 31 (12) (2021) 2008586, https://doi.org/10.1002/adfm.202008586.
[15] S. Wang, Q.X. Shi, Y.S. Ye, Y. Xue, Y. Wang, H.Y. Peng, X.L. Xie, Y.W. Mai, Constructing desirable ion-conducting channels within ionic liquid-based composite polymer electrolytes by using polymeric ionic liquid-functionalized 2D mesoporous silica nanoplates, Nano Energy 33 (2017) 110–123, https://doi.org/10.1016/j.nanoen.2017.01.036.
[16] Y. Shi, Z. Fan, B. Ding, Z. Li, Q. Lin, S. Chen, H. Dou, X. Zhang, Atomic-scale Al2O3 modified PEO-based composite polymer electrolyte for durable solid-state Li − S batteries, J. Electroanal. Chem. 881 (2021) 114916, https://doi.org/10.1016/j.jelechem.2020.114916.
[17] Z. Cui, V. Marangon, J. Hassoun, Y. Tominaga, Polycarbonate-based composite polymer electrolytes with Al2O3 enhanced by in situ polymerized electrolyte Interlayers for all-solid-state lithium-metal batteries, J. Power Sources 611 (2024) 234760, https://doi.org/10.1016/j.jpowsour.2024.234760.
[18] Z. Fang, M. Zhao, Y. Peng, S. Guan, Poly (vinylidene fluoride) binder reinforced poly (propylene carbonate)/3D garnet nanofiber composite polymer electrolyte toward dendrite-free lithium metal batteries, Mater. Today Energy 24 (2022) 100952, https://doi.org/10.1016/j.mtener.2022.100952.
[19] W. Kou, J. Wang, W. Li, R. Lv, N. Peng, W. Wu, J. Wang, Asymmetry-structure electrolyte with rapid Li+ transfer pathway towards high-performance all-solid-state lithium–sulfur battery, J. Membr. Sci. 634 (2021) 119432, https://doi.org/10.1016/j.memsci.2021.119432.
[20] S. Li, L. Li, H. Yang, Y. Zhao, Y. Shan, A review of composite polymer electrolytes for solid-state lithium-sulfur batteries: synthesis methods, optimal design, and critical challenges, Chem. Eng. J. 484 (2024) 149433, https://doi.org/10.1016/j.cej.2024.149433.
[21] Y.S. Ye, M.G. Mohamed, N.H. Ye, T.Y. Hung, G.Y. Chen, S.H. Lin, M.C. Tsai, B. J. Hwang, S.W. Kuo, Single-atom catalyst-integrated porous organic polymers for high-performance lithium-sulfur batteries, Small 21 (32) (2025) e2503250, https://doi.org/10.1002/smll.202503250.
[22] Y.S. Ye, M.G. Mohamed, W.C. Chen, S.W. Kuo, Integrating the multiple functionalities in metalloporphyrin porous organic polymers enabling strong polysulfide anchoring and rapid electrochemical kinetics in Li-S batteries, J. Mater. Chem. A 11 (16) (2023) 9112–9124, https://doi.org/10.1039/d2ta09232h.
[23] G. Raj Deivendran, S.-H. Wu, Y.-S. Wu, J.-K. Chang, R. Jose, K.H. Ng, M. Poddar, C.-L. Sun, C.-C. Yang, Suppression of polysulfides by carbonized polyacrylonitrile modified polypropylene Janus separator for Li2S/r-GONR/CNT-based Li–S batteries, ACS Appl. Energy Mater. 7 (8) (2024) 3321–3338, https://doi.org/10.1021/acsaem.4c00093.
[24] Y.-H. Liu, L.-X. Li, A.-Y. Wen, F.-F. Cao, H. Ye, A Janus MXene/MOF separator for the all-in-one enhancement of lithium-sulfur batteries, Energy Storage Mater. 55 (2023) 652–659, https://doi.org/10.1016/j.ensm.2022.12.028.
[25] Z. Zhang, Y. Dong, Y. Gu, P. Lu, F. Xue, Y. Fan, Z. Zhu, J. Lin, Q. Li, Z.-S. Wu, Graphene-nanoscroll-based Janus bifunctional separators suppress lithium dendrites and polysulfides shuttling synchronously in high-performance lithium–sulfur batteries, J. Mater. Chem. A 10 (17) (2022) 9515–9523, https://doi.org/10.1039/D2TA01515C.
[26] H. Pei, C. Yang, Q. Wu, X. Zhou, X. Xie, B. Hwang, Y. Ye, Ion-selective aramid nanofiber-based Janus separators fabricated by a dry-wet phase inversion approach for lithium–sulfur batteries, J. Mater. Chem. A 10 (10) (2022) 5317–5327, https://doi.org/10.1039/D1TA09533A.
[27] C. Chang, C. Yang, Q. Wu, X. Wang, H. Nie, X. Zhou, X. Xie, B. Hwang, Y. Ye, All-in-one Janus separator for lithium–sulfur batteries with lithium polysulfide and dendrite growth suppressed at temperature gradient effect, J. Power Sources 550 (2022) 232115, https://doi.org/10.1016/j.jpowsour.2022.232115.
[28] J. Wang, X. Yan, Z. Zhang, R. Guo, H. Ying, G. Han, W.-Q. Han, Rational design of an electron/ion dual-conductive cathode framework for high-performance all-solid-state lithium batteries, ACS Appl. Mater. Interfaces 12 (37) (2020) 41323–41332, https://doi.org/10.1021/acsami.0c10463.
[29] Z. Li, J. Zhang, X.W. Lou, Hollow carbon nanofibers filled with MnO2 nanosheets as efficient sulfur hosts for lithium–sulfur batteries, Angew. Chem. Int. Ed. 54 (44) (2015) 12886–12890, https://doi.org/10.1002/anie.201506972.
[30] W. Kong, L. Yan, Y. Luo, D. Wang, K. Jiang, Q. Li, S. Fan, J. Wang, Ultrathin MnO2/graphene oxide/carbon nanotube interlayer as efficient polysulfide-trapping shield for high-performance Li–S batteries, Adv. Funct. Mater. 27 (18) (2017) 1606663, https://doi.org/10.1002/adfm.201606663.
[31] Z. Cai, L. Xu, M. Yan, C. Han, L. He, K.M. Hercule, C. Niu, Z. Yuan, W. Xu, L. Qu, K. Zhao, L. Mai, Manganese oxide/carbon yolk–shell nanorod anodes for high capacity lithium batteries, Nano Lett. 15 (1) (2015) 738–744, https://doi.org/10.1021/nl504427d.
[32] Z.-Y. Tian, P. Mountapmbeme Kouotou, N. Bahlawane, P.H. Tchoua Ngamou, Synthesis of the catalytically active Mn3O4 spinel and its thermal properties, J. Phys. Chem. C 117 (12) (2013) 6218–6224, https://doi.org/10.1021/jp312444s.
[33] Y. Zhu, Y. Zuo, X. Jiao, R. Manjunatha, E.R. Ezeigwe, W. Yan, J. Zhang, Selective sulfur conversion with surface engineering of electrocatalysts in a lithium–sulfur battery, Carbon Energy 5 (2) (2023) e249, https://doi.org/10.1002/cey2.249.
[34] Y. Cui, J. Wan, Y. Ye, K. Liu, L.-Y. Chou, Y. Cui, A. Fireproof, Lightweight, polymer–polymer solid-state electrolyte for safe lithium batteries, Nano Lett. 20 (3) (2020) 1686–1692, https://doi.org/10.1021/acs.nanolett.9b04815.

[35] J. Wan, J. Xie, X. Kong, Z. Liu, K. Liu, F. Shi, A. Pei, H. Chen, W. Chen, J. Chen, X. Zhang, L. Zong, J. Wang, L.-Q. Chen, J. Qin, Y. Cui, Ultrathin, flexible, solid polymer composite electrolyte enabled with aligned nanoporous host for lithium batteries, Nat. Nanotechnol. 14 (7) (2019) 705–711, https://doi.org/10.1038/s41565-019-0465-3.

[36] Y.-H. Lin, W.-M. Huang, J.-Y. Li, M.G. Mohamed, C.-Y. Tseng, J.-M. Chiu, B.-J. Hwang, S.-W. Kuo, Y.-S. Ye, Nonsolvent-induced phase separation polyimide/polymeric ionic liquid separators for high-performance and safe lithium metal-based batteries, J. Membr. Sci. 728 (2025) 124125, https://doi.org/10.1016/j.memsci.2025.124125.

[37] J. Liu, C. Chen, Y. Feng, Y. Liao, Y. Ye, X. Xie, Y.W. Mai, Ultralow-carbon nanotube-toughened epoxy: the critical role of a double-layer interface, ACS Appl. Mater. Interfaces 10 (1) (2018) 1204–1216, https://doi.org/10.1021/acsami.7b14767.

[38] A. Saleem, R. Iqbal, M.K. Majeed, A. Hussain, A.R. Akbar, Z. Hussain, B. Jabar, S. Rauf, L.L. Shaw, Boosting lithium-ion conductivity of polymer electrolyte by selective introduction of covalent organic frameworks for safe lithium metal batteries, Nano Energy 128 (2024) 109848, https://doi.org/10.1016/j.nanoen.2024.109848.

[39] V. Marangon, D. Di Lecce, L. Minnetti, J. Hassoun, Novel lithium-sulfur polymer battery operating at moderate temperature, ChemElectroChem 8 (20) (2021) 3971–3981, https://doi.org/10.1002/celc.202101272.

[40] J. Feng, J. Wang, Q. Gu, P. Li, H. Xu, Y. Deng, P. Gao, 1 μm-Thick robust gel polymer electrolyte with excellent interfacial stability for high-performance Li metal batteries, Adv. Funct. Mater. 35 (2) (2025) 2412287, https://doi.org/10.1002/adfm.202412287.

[41] J.-Q. Huang, Q. Zhang, F. Wei, Multi-functional separator/interlayer system for high-stable lithium-sulfur batteries: progress and prospects, Energy Storage Mater. 1 (2015) 127–145, https://doi.org/10.1016/j.ensm.2015.09.008.

[42] Z. Ji, L. Feng, Z. Zhu, X. Fu, W. Yang, Y. Wang, Polymeric interface engineering in lithium-sulfur batteries, Chem. Eng. J. 455 (2023) 140462, https://doi.org/10.1016/j.cej.2022.140462.

[43] C. Ye, Y. Jiao, H. Jin, A.D. Slattery, K. Davey, H. Wang, S.-Z. Qiao, 2D MoN-VN heterostructure to regulate polysulfides for highly efficient lithium-sulfur batteries, Angew. Chem. Int. Ed. 57 (51) (2018) 16703–16707, https://doi.org/10.1002/anie.201810579.

[44] Y.-X. Song, Y. Shi, J. Wan, S.-Y. Lang, X.-C. Hu, H.-J. Yan, B. Liu, Y.-G. Guo, R. Wen, L.-J. Wan, Direct tracking of the polysulfide shuttling and interfacial evolution in all-solid-state lithium–sulfur batteries: a degradation mechanism study, Energy Environ. Sci. 12 (8) (2019) 2496–2506, https://doi.org/10.1039/C9EE00578A.

[45] R. Fang, H. Xu, B. Xu, X. Li, Y. Li, J.B. Goodenough, Reaction mechanism optimization of solid-state Li–S batteries with a PEO-based electrolyte, Adv. Funct. Mater. 31 (2) (2021) 2001812, https://doi.org/10.1002/adfm.202001812.

[46] K. Xu, X. Liu, J. Liang, J. Cai, K. Zhang, Y. Lu, X. Wu, M. Zhu, Y. Liu, Y. Zhu, G. Wang, Y. Qian, Manipulating the redox kinetics of Li–S chemistry by tellurium doping for improved Li–S batteries, ACS Energy Lett. 3 (2) (2018) 420–427, https://doi.org/10.1021/acsenergylett.7b01249.

[47] Y. Huang, M. Shaibani, T.D. Gamot, M. Wang, P. Jovanović, M.C. Dilusha Cooray, M.S. Mirshekarloo, R.J. Mulder, N.V. Medhekar, M.R. Hill, M. Majumder, A saccharide-based binder for efficient polysulfide regulations in Li-S batteries, Nat. Commun. 12 (1) (2021) 5375, https://doi.org/10.1038/s41467-021-25612-5.

[48] R. Meng, Q. Du, N. Zhong, X. Zhou, S. Liu, S. Yin, X. Liang, A tandem electrocatalysis of sulfur reduction by bimetal 2D MOFs, Adv. Energy Mater. 11 (47) (2021) 2102819, https://doi.org/10.1002/aenm.202102819.

[49] Y.S. Ye, M.G. Mohamed, M.C. Tsai, H.Y. Hu, B.J. Hwang, S.W. Kuo, Crown ether functionalized large-area graphene oxide and MXene hybridize as ion-sieving layers for high-performance lithium-sulfur batteries, J. Mater. Chem. A 12 (37) (2024) 25346–25358, https://doi.org/10.1039/d4ta04005h.

[50] Q. Liang, S. Wang, Y. Yao, P. Dong, H. Song, Transition metal compounds family for Li–S batteries: the DFT-guide for suppressing polysulfides shuttle, Adv. Funct. Mater. 33 (32) (2023) 2300825, https://doi.org/10.1002/adfm.202300825.

[51] J. Song, M.L. Gordin, T. Xu, S. Chen, Z. Yu, H. Sohn, J. Lu, Y. Ren, Y. Duan, D. Wang, Strong lithium polysulfide chemisorption on electroactive sites of nitrogen-doped carbon composites for high-performance lithium-sulfur battery cathodes, Angew. Chem. 54 (14) (2015) 4325–4329.

[52] L. Mao, Y. Zou, R. Yang, C. Fan, X. Dong, Y. Yan, L. Zhong, Y. Xu, Advances in the density functional theory (DFT) calculation of lithium-sulfur battery cathodes, Mater. Today Commun. 36 (2023) 106814, https://doi.org/10.1016/j.mtcomm.2023.106814.